This is a preprint, the final version is subject to change, of the American Mineralogist (MSA)
Cite as Authors (Year) Title. American Mineralogist, in press.
DOI: https://doi.org/10.2138/am-2019-6730

REVISION #2

Lead diffusion in $CaTiO_3$: A combined study using Rutherford Backscattering and TOF-SIMS for depth profiling to reveal the role of lattice strain in diffusion processes

Christopher Beyer[1], Ralf Dohmen[1], Detlef Rogalla[2], Hans-Werner Becker[2], Katharina Marquardt[3], Christian Vollmer[4], Ulrich Hagemann[5,6], Nils Hartmann[5,6,7], Sumit Chakraborty[1,2]

[1]Institut für Geologie, Mineralogie und Geophysik, Ruhr-Universität Bochum, Bochum, Germany

[2]RUBION, Ruhr-Universität Bochum, Bochum, Germany

[3]Bayerisches Geoinstitut, Universität Bayreuth, Bayreuth, Germany

[4]Institut für Mineralogie, Westfälische Wilhelms-Universität Münster, Münster, Germany

[5]Interdisciplinary Centre for Analytics on the Nanoscale, Universität Duisburg-Essen, Duisburg, Germany

[6]Centre for Nanointegration Duisburg-Essen (CENIDE), Universität Duisburg-Essen, Duisburg, Germany

[7]Fakultät für Chemie, Universität Duisburg-Essen, Duisburg, Germany

Abstract

We present experimental data on the diffusivity of Pb in $CaTiO_3$ perovskite, which is commonly used for dating kimberlites and carbonatites. Experiments were performed on oriented synthetic and natural $CaTiO_3$ single crystals. The Pb-source was either a laser deposited $(Ca_{0.83}Pb_{0.07})Ti_{1.05}O_3$ thin film or a $(Ca_{0.9}Pb_{0.1})TiO_3$ powder reservoir. The crystals were annealed in a high-temperature furnace between 736 and 1135°C and

for durations from 2 to 283 hours. The diffusion profiles were measured with Rutherford back-scattering and time-of-flight secondary ion mass spectrometry in the depth-profiling mode. The concentration profiles measured on the same samples with the two analytical methods are in agreement. The measured concentration profiles show two regions - a steep gradient at the diffusion interface that transitions sharply (at ~ 50 to 150 nm from the surface) to a low concentration tail that penetrates deeper into the crystal. This diffusion behavior could be modelled best using diffusion coefficients that are a function of the Pb concentration, with a different set of diffusion coefficient for the high and the low concentration region of the profile, respectively. The diffusion coefficients extracted from the thin film and powder source experiments are similar within uncertainties. Pb diffuses slower at concentrations between 8.5 and 0.6 wt.% and 1.6 to 2.6 log units faster below ~ 0.5 wt.% Pb. Temperature dependency for each region is discussed in the text, and the Arrhenius relation for the fast diffusion regime that is most relevant for natural samples is

$$D_{Pb}^{fast} = 2.5 * 10^{-13} * \exp(-158(24) kJ/mol/RT)\, m^2/s.$$

We found a distinct change in the structure of $CaTiO_3$ in the surface region of the single crystal that is coincidental with the change in diffusivity. This initial region is dominated by planar defects. We propose that Pb is trapped in planar defects that have formed due to the high strain introduced into the perovskite structure caused by the mismatch in the ionic radius between Ca^{2+} and Pb^{2+}. The activation energies obtained here yield closure temperature for Pb in $CaTiO_3$ between 300 and 400 °C for a range of different cooling scenarios, if diffusive resetting of Pb in $CaTiO_3$ occurs at all. At typical cooling rates of hours to days for ascending kimberlite, the age of crystal growth is preserved, with closure temperatures similar to the magma temperature.

Keywords: *perovskite, diffusion, experimental, lattice strain, closure temperature, U/Pb chronometry*

Introduction

Perovskite (ABO_3) is an important mineral group that crystallizes in the groundmass of various eruptive alkaline rocks such as kimberlites, lamproites and carbonatites (Edgar and Mitchell 1997; Mitchell et al. 2017). Its different modifications are present in the Earth's upper mantle ($CaTiO_3$) as well as in the lower mantle, either as calcium perovskite ($CaTiO_3$, $CaSiO_3$) or as bridgmanite ($[Mg,Fe]SiO_3$). Due to the flexibility of the perovskite structure, calcium perovskite is known to concentrate light rare earth elements, high field strength elements, large ion lithophile elements, uranium and thorium (Veksler and Teptelev 1990; Chakhmouradian and Mitchell 2001; Corgne and Wood 2002; Beyer et al. 2013). Many functional materials have a perovskite structure and are used in fuel cells, solar cells, catalysts and high-temperature super conductors (Bednorz and Müller 1986; Goodenough 2004; Huang et al. 2006; Hodes 2013; Kühl et al. 2017). The eponymous $CaTiO_3$ is used for dating (U/Th-Pb) and isotopic finger printing (Sr, Nd) in high-alkaline rocks, where other phases typically used for dating (i.e. garnet, zircon, monazite) are rare or absent (Kramers and Smith 1983; Smith et al. 1989; Heaman 1989, 2009; Tappe and Simonetti 2012). An advantage of perovskite is its high concentration of U (10 – 300 ppm) and Th (up to 10000 ppm), leading to high concentrations of radiogenic Pb (Heaman et al. 2003). The maximum amount of Pb in natural $CaTiO_3$ is on the order of a few hundred ppm (Chakhmouradian et al. 2013). Depending on its magmatic history, perovskite shows distinct core-to-rim variations in rare earth elements, U, Th and Pb-concentrations (Reguir et al. 2010; Chakhmouradian et al. 2013).

$CaTiO_3$ undergoes phase transitions from *Pbnm* to *Cmcm* at 1117 °C, to *I4/mcm* at 1227 °C and to $Pm\bar{3}m$ at 1307 °C (Kennedy et al. 1999). It forms a complete solid solution with $PbTiO_3$, where Ca^{2+} (1.34 Å) is replaced by Pb^{2+}(1.49 Å) on the A-site. The solid solution $(Ca_xPb_{1-x})TiO_3$ is accompanied by a change in the crystal structure from orthorhombic (*Pbnm*) to tetragonal (*P4mm*) at $x \leq 0.416$ forming a morphotrophic phase boundary (Chandra and Pandey 2011).

So far, only one study empirically estimated the closure temperature of Pb in perovskites to lie between 790 to 900 °C for 30 - 50 µm grain size and cooling rates between 10 °C/Myr and 200 °C/Myr. However, these closure temperatures are based on the concept of ionic porosity (Zhao and Zheng 2007) and are not verified

by experimentally derived diffusion parameters. Hence, in this study we performed diffusion experiments on synthetic and natural perovskite single crystals to quantify experimentally the diffusive behavior of Pb in $CaTiO_3$ for the first time. The results serve as a model study on how lattice strain effects may alter the mechanism and rates of diffusion. The Arrhenius relation obtained in this study has been used to calculate the closure temperature for Pb and is useful for constraining the timescale of emplacement and cooling of kimberlites and carbonatites based on core-to-rim zonation of Pb in natural $CaTiO_3$ grains. This experimental work serves in addition as a comparison between two types of setups and analytical methods used for diffusion studies: Thin-film diffusion experiments vs. powder source diffusion experiments (e.g., see Watson and Dohmen (2010)) and Rutherford backscattering (RBS) and time-of-flight secondary ion mass spectrometry (TOF-SIMS).

Experimental Methods

We used synthetic and natural perovskite single crystals. The synthetic, crystallographically oriented $CaTiO_3$ single crystals were provided by SurfaceNet GmbH (Electronic Annex Table A3). The crystals were cut in ~ 1.5 x 1.5 x 1.0 mm cubes. The (100) surface was mechanically polished using diamond pastes and alumina colloid compounds. The natural $CaTiO_3$ was sourced from Zlatoust, Ural, Russia (Electronic Annex Table A3). The natural crystals were cut in ~ 2.0 x 2.0 x 2.0 mm cubes with random orientation and polished in the same manner. Natural crystals are opaque and contain several hundred ppm of different trace elements.

As the source for the diffusion experiments we synthesized powders with the stoichiometric composition $(Ca_{0.9}Pb_{0.1})TiO_3$ and $(Ca_{0.8}Pb_{0.2})TiO_3$ from pure $CaTiO_3$ and $PbTiO_3$. These two end-member compositions were made by mixing analytical grade $CaCO_3$ (purity 99.5%), PbO (99.999 %) and TiO_2 (99.8 %). 5 wt.% of PbO was added to the starting composition in excess to account for Pb-loss during annealing. The reagents composing each end-member were blended and thoroughly ground with acetone in an agate mortar. Subsequently, the mixture containing $CaCO_3$ was calcinated at 1000 °C for 6 hours. $CaTiO_3$ and $PbTiO_3$

were heated at 1100 and 900 °C, respectively, to obtain the orthorhombic ($CaTiO_3$) and tetragonal ($PbTiO_3$) perovskite structure. The structure has been confirmed by powder x-ray diffraction in each case. The final mixture was prepared by mixing these perovskite end-members and heating the mixture at 900 °C for 20 hours to obtain a solid solution.

Two types of diffusion experiments were performed. (i) Powder source experiments were conducted (a summary of the method is described in Watson and Dohmen (2010), for example) with the $(Ca_{0.9}Pb_{0.1})TiO_3$ powder as an infinite source for Pb. Crystals were loaded into alumina crucibles filled with the finely ground powder. The crucibles were covered with a tight fitting lid cast from fired pyrophyllite to reduce the evaporation of Pb. (ii) Thin film diffusion couples were prepared by pulsed laser ablation of pellets with the composition $(Ca_{0.8}Pb_{0.2})TiO_3$. We used an excimer laser with 193 nm wave length and an energy of about 200 mJ, pulsed with 10 Hz for 4 minutes. The $CaTiO_3$ substrates were heated to ~ 400 °C in a vacuum at $6*10^{-3}$ bar. Details of the experimental setup and routine are provided in Dohmen et al. (2002).

Diffusion anneals were conducted in a vertical tube furnace and in a box furnace at atmospheric pressure. The temperature was monitored with a B-Type thermocouple, placed within 2 cm of the sample container. The samples were annealed for 2 to 283 hours. Experimental conditions are reported in Table 1. The recovered samples were cleaned and examined qualitatively under reflected light before they were quantitatively analyzed using RBS and TOF-SIMS.

Some test annealing runs were carried out at an oxygen fugacity of -0.5 log units relative to the nickel – nickel oxide buffer conditions ($fO_2 = 10^{-8}$ bar at 834 °C, ~NNO = -0.5), set with a continuous CO-CO_2 gas flow. At these conditions Pb^{2+} is reduced to Pb^0 in the gas phase and evaporates quickly; hence, it was not possible to measure any profile at reducing conditions. Analysis of the experiments carried out at reducing conditions lost all Pb and the $(Ca,Pb)TiO_3$ transformed to $CaTiO_3$ and TiO_2 which was confirmed by powder x-ray diffraction.

Analytical Methods

Rutherford back-scattering (RBS)

Samples from both types of diffusion experiments were investigated using RBS, which permits obtaining depth resolved element analysis of the near-surface regions (roughly, the uppermost micrometer). Numerous studies demonstrated that RBS is well-suited for measuring depth profiles of heavy elements, (in this case Pb) in a light matrix (e.g. oxides and silicates) (Jaoul et al. 1991; Cherniak 2000; Cherniak and Watson 2001). RBS spectra were measured at the 4 MV Dynamitron Tandem Accelerator of the Ruhr-Universität Bochum. A 2 MeV ^{4}He beam is focused onto the sample surface using a 0.5 mm diameter aperture yielding a beam area of 1 mm². Beam current was varied between 20 and 50 nA. The sides of the samples were wrapped with Al-foil to minimize charging of the sample surface. Back-scattered particles are detected at an angle of 160°. The solid-state silicon detector has a resolution of 18 to 22 keV. Samples were tilted with an angle between 5° and 20° relative to the incident beam to avoid channeling. Pb depth profiles were extracted from the RBS spectrum using the software package RBX, version 5.18 (Kótai 1997). More details of the setup and the fitting procedure are given, for example, in Dohmen et al. (2002).

Time of Flight Secondary Ion Mass Spectrometry (TOF-SIMS)

We measured additional diffusion profiles of the same samples with TOF-SIMS because RBS has limitations in terms of sensitivity (100s ppm) and observable profile length. The latter is caused by the overlap of the Pb signal from depths greater than 500 nm with the signal from lighter elements near the surface. The advantages of TOF-SIMS are a higher sensitivity in the sub-ppm range and a depth resolution of 3 nm based on the reference sample. Analyses were carried out with an TOF.SIMS 5-100 from IONTOF at the Interdisciplinary Center of Analytics on the Nanoscale (ICAN) at the University of Duisburg-Essen. Samples were sputter etched on a 300 x 300 μm^2 area with a microfocused O_2^+ secondary ion beam at 2 kV. A 30kV microfocused primary Bi_1^+ beam, was used in non-interlaced method for analysis of a 100 x 100

μm^2 area in the center of the sputtered crater. The pulse width of the primary beam was varied between 6 and 30 ns to improve the ion yield. Charging was compensated by adjusting an oxygen background pressure of $3x10^{-7}$ mbar in the analysis chamber and using a flood gun to compensate surface charging. The spectra were reconstructed using the time-of-flight correction, as implemented in IONTOF measurement explorer version 6.5. We used at least 13 known peaks (e.g. C^+, CH^+, CH_3^+, Na^+, Ca^+, Ti^+, CaO^+, TiO^+, Ca^{++}, $Ti_2O_2^+$, $^{206}Pb^+$,$^{207}Pb^+$,$^{208}Pb^+$), covering the mass range from 1 to 208 atomic mass units (a.m.u.), for the mass calibration of the spectra. The intensity of the sum of $^{204}Pb^+$, $^{206}Pb^+$, $^{207}Pb^+$ and $^{208}Pb^+$ signals were normalized at each point to the total intensity. The resulting intensity vs. sputtering time profiles were then extracted for subsequent data treatment. Beam currents were measured before and after the data acquisition. For the short measurement times, usually shorter than 1 hour, the beam currents were stable within 1 %. TOF-SIMS intensities were calibrated using the RBS data in order to obtain concentrations. RBS data reveals Pb concentrations from 2.2 to 8.5 wt.% at the surface.

The depth of the TOF-SIMS craters was determined using an interference microscope (IFM) supplied by ATOS. The wave-mode was employed to collect interference pattern of the crystal surface. Assuming a linear relationship between sputtering time and sputtering rate we established a linear function to calculate the crater depth, where measurements with the IFM were not feasible (samples Pv_Pb_26n). At least four depth profiles per crater were collected and the average depth was used for subsequent calculations. The reproducibility of the crater depths was usually better than 25 nm.

Transmission electron microscopy (TEM)

One synthetic sample (Pv_Pb_29) has been investigated further to identify any possible microstructures that may have had a potential effect on diffusion (e.g. grain boundaries, twins, lattice defects, and exsolution lamellae). We prepared two electron-transparent lamellae with approximate dimensions of 25 by 15 μm^2 and lamella thickness varying between 5 and 100 nm using a FEI Scios Focused Ion Beam Scanning Electron Microscope. The rough milling was performed at an acceleration voltage of 30 kV and the beam

current was varied from 7 nA down to 100 pA. Since the amorphous damage layer produced on the lamella surfaces dependent on beam energy, we used a final polishing step at reduced acceleration voltage following suggestions of Yabusaki and Sasaki (2002) and Schaffer et al. (2012) at an acceleration voltage between 5 and 2 kV and currents of 4 up to 100 pA for approximately one minute.

Analyses by transmission electron microscopy (TEM) were carried out on three different microscopes at the University of Münster and the Bayerisches Geoinstitut. Initial characterization was performed on a Zeiss Libra 200FE with an acceleration voltage of 200 kV (Schottky field emission gun) and strongly parallel Köhler illumination conditions. All bright field (BF) and selected area electron diffraction (SAED) imaging were performed in energy filtered mode with the energy-selecting slit (~30 eV width) centered on the zero loss peak using an in-column Omega filter on a Gatan UltraScan 4k×4k CCD camera. Z-contrast imaging was performed in scanning TEM (STEM) mode using a 20 µm condenser aperture on a high angle annular dark-field (HAADF) detector. The spot size with these settings was about 2 nm. Further high-resolution imaging and EDX mapping were performed on a FEI/ThermoFisher Titan "Themis" with an acceleration voltage of 300 kV and a C_s (spherical aberration)- corrected objective system. The size of the objective aperture was set to 60 µm for high resolution imaging and 30 µm for BF imaging on an ultrafast 4kx4k CMOS sensor. EDX mapping was performed in STEM mode using a 50 µm condenser aperture and a four-quadrant peltier-cooled silicon drift detector (ChemiSTEM technology) on the Themis at the University of Münster.

Results

Recovered crystals were free of surface alterations, such as etch pits. Residual powder stuck to the surface in some of the high temperature powder source experiments but the relative area covered by such powder was always below 1%. Most of the powder was removed by suspending the sample in an ultrasonic bath. The recovered powders were slightly more yellow compared to the pale yellow powder before the experiment. Arbitrarily chosen powders were examined with XRD to confirm that the recovered material

was still a (Ca,Pb)TiO_3 solid solution. We found trace amounts of rutile, probably formed by the partial loss of Pb by evaporation (Figure 1a). Assuming rapid chemical communication among phases in the system the formation of rutile buffers the system in terms of the chemical potential of TiO_2.

Rutherford back-scattering spectroscopy

Stoichiometry and thickness of the thin-film samples prior to the experiments was measured on the reference sample Pv_Pb_13 by using RBS. We found that the film had a deficit in Pb yielding a composition of $(Ca_{0.83}Pb_{0.07})Ti_{1.05}O_3$. The stoichiometry is based on the assumption that all oxygen lattice positions are fully occupied and Pb is primarily present as Pb^{2+}. The thickness was determined to be 80(5) nm. Based on previous studies with the same equipment we expect all deposited films to have the same composition. (e.g. see Dohmen et al. 2002). The thickness is assumed to be within 10 % of the reference value (Dohmen et al. 2002). Combining the uncertainty in thickness (~ 8 nm) with the resolution limit of RBS (5 nm) we expect to have a maximum variation of 13 nm in thickness.

After the diffusion anneal we found that the Pb peak within the film was reduced compared to the reference sample, which we attribute to two fluxes: (i) Diffusive flux from the thin film into the perovskite substrate as measured by the Pb concentration gradient below the film. This flux can be also inferred from the shape of the high-energy side of the Pb peak (i.e. the surface region) in the RBS spectrum (Figure 1a). In addition, we observed a change in the gradient at lower Pb-concentrations (Figure 1b), indicating the diffusion into the sample, albeit most of the tailing profile is superimposed by the signal background.

We forward modeled the depth profiles of the thin film and powder source anneals using a numerical finite difference scheme (Crank 1979). A detailed outline and description of this method is given in Costa et al. (2008), for example.

Time-of-flight secondary ion mass spectrometry

The profiles have a steep gradient close to the surface of the crystal within the first 30 to 200 nm and a shallow gradient along the low concentration tail that penetrates deeper into the crystal. The transition between the two regions is marked by a distinct kink in the profile (Figure 2a-d). We could not unambiguously measure the low concentration tail (e.g., as shown in the inset of Fig. 1b) using RBS because of the limitations mentioned above. Therefore, we analyzed the same samples with TOF-SIMS as well in order to determine the entire profile, including the tail, until the Pb signal leveled out at a constant signal intensity. TOF-SIMS is only semi-quantitative and so for better comparability the signal intensity was normalized to the value of the concentration at the surface that was obtained by RBS.

Modelling the concentration profiles

We used an empirical model that accounts for the dependence of diffusivity on the concentration of the diffusant:

$$D_{Pb} = D_{Pb}^{fast} + D_{Pb}^{slow} * \exp\left[-\left(\frac{C_{Pb}}{C_{crit}}\right)^{a}\right] \quad (1)$$

where D_{Pb}^{fast} and D_{Pb}^{slow} are the diffusion coefficients at the tail and near the surface, respectively. C_{crit} is the critical concentration where the diffusion regime changes and the parameter a controls the sharpness of the transition from D_{Pb}^{slow} to D_{Pb}^{fast}, although neither of these terms is rooted in atomistic theory (Dohmen et al. 2018). We employed an explicit numerical algorithm, based on the forward-time-central-space (FCTS) scheme, to solve the diffusion equation (Crank 1979) . For the thin film samples, we started off with an initial step profile and zero flux at the crystal surface. The powder source experiments were treated as an open system with a constant Pb concentration at the surface.

Results of the fitting-by-eye are given in Figure 2 and calculated Ds are reported in Table 2. The reproducibility of the fitting is usually better than 0.1 log units, which is below the run-to-run reproducibility of the experiments (Dohmen et al. 2016).

Diffusion coefficients of Pb and their temperature dependence

D_{Pb}^{slow} from the TOF-SIMS profiles is identical within uncertainties to D_{Pb}^{RBS} ,extracted by fitting the steeper part of the RBS profiles (Figure 3, Table 2). The parameter a varies between 0.6 and 1.5 and the critical concentrations were determined to lie between 152 µg/g and 7268 µg/g Pb. All profiles have in common that at the critical concentration C_{crit} the rate of diffusion increased significantly by 1.6 to 2.6 log units, with the exception of run# Pv_Pb_23, where the diffusivity only increased by 0.5 log units. Diffusion coefficients from randomly oriented natural crystals, which are free of any macroscopic inlusions, (Pv_Pb_21 and Pv_Pb_26n) are in very good agreement with diffusion coefficients obtained from synthetic crystals oriented perpendicular to (100) (diamonds in Figure 4), strongly suggesting that perovskite is isotropic with respect to Pb-Ca interdiffusion.

The diffusion data obtained here are consistent although different methods were used to create the diffusion profiles (thin film on synthetic crystal, powder source with synthetic crystal and powder source with natural crystal). We therefore conclude that the experimental and analytical methods used do not introduce any artifacts. Consequently, we combined all diffusion coefficients in an Arrhenius diagram to obtain the pre-exponential factor D_0 and activation energy E_a (Figure 4, Table 3). The activation energies E_a for Pb in $CaTiO_3$ calculated from the Arrhenius relation are 133(13) kJ/mol for D_{Pb}^{RBS}, 139(32) kJ/mol for D_{Pb}^{slow} and 158(24) kJ/mol for D_{Pb}^{fast}. We found that E_a is similar within error for RBS and TOF-SIMS.

Time series

The experiments Pv_Pb_24, Pv_Pb_28, Pv_Pb_30 and Pv_Pb_31 were all performed at similar temperature of 964 to 970 °C (Table 2) and should yield similar diffusion coefficients if we measured volume diffusion. The duration of the anneals were varied between 19 and 283 hours. The slow diffusion mechanism is in mutual agreement within 0.3 log units, whereas, the fast diffusion mechanism shows a slightly worse

reproducibility with 0.6 log units (Figure 5). We can only speculate what the reason is. The most obvious explanation is the very low count rates along the low concentration tail, which lead to noisier profiles.

Microstructural observations

We analyzed two FIB-lamellae extracted from the powder source experiment Pv_Pb_29 (concentration profile is shown in Figure 3), cut normal to the crystal surface. In order to confirm that the different regions are perovskite, we collected selected area diffraction (SAD) patterns. The unit cell extracted from all patterns is that of orthorhombic $CaTiO_3$ with a = 5.37 Å and b = 5.44 Å along the zone axis [001].

We applied TEM-BF and STEM-HAADF imaging to check for potential path-ways such as dislocations and sub-grain boundaries that might explain the change in diffusion rates (Figure 6). (i) We found planar defects in the uppermost 100 - 150 nm; (ii) the bulk of the crystal is free of planar defects and contains voids in the shape of idiomorphic $CaTiO_3$ crystals, possibly caused by condensation of excess vacancies; (iii) the parallel features, that are visible on the surface (Figure A2), are twin-boundaries, similar to the boundaries described by Rothmann et al. (2017) in tetragonal perovskite. However, these twin boundaries are most likely not responsible for the change in diffusivity in the uppermost layer (see discussion).

The area that comprises a higher density of dislocations also coincides with the high Pb-concentration – slow diffusivity region. The EDS-maps of Ca and Pb (Figure 6d) illustrated an increased Pb-concentration in the first 10s of nm of the diffusion interface. In some regions, where the defects originate in proximity to the surface, we see an even higher concentration of Pb (Figure 6d), which we associate to the origin of the defects.

Discussion

We observed two characteristic features of Pb diffusion in perovskite that are unusual compared to diffusion behavior of cations in oxides and silicates: (i) diffusion rates depend on concentration of Pb, and change by

two orders of magnitude when Pb concentration increases from trace element to minor element levels, and (ii) the activation energy of ~ 150 kJ/mol is relatively low and lies at the lower end of experimentally determined activation energies for divalent cations in minerals, most of which are, however, silicates and oxides (e.g., see Fig. 13 in Brady and Cherniak (2010)). For example, these low activation energies are similar to those obtained for Sr diffusion in F-phlogopite (Hammouda and Cherniak 2000). The only other directly measured diffusion data that are known for $CaTiO_3$ are for O diffusion, where a much higher activation energy of ~ 300 kJ/mol was found (Gautasson and Muehlenbachs 1993; Sakaguschi and Haneda 1996) (Figure 8). Bak et al. (2004a) inferred chemical diffusion rates (volume diffusion) in $CaTiO_3$ from electrical conductivity data and found an activation energy of 134 kJ/mol at fO_2 of $1e^{-4}$ bar, which is in excellent agreement with our results. However, they also inferred a much lower activation energy of 66 kJ/mol only at 100% oxygen flow ($fO_2 = 7.2e^{-4}$ bar), where $CaTiO_3$ is in the p-type regime, and similarly, George and Grace (1969) inferred an even lower activation energy of ~22 kJ/mol. However, these data are based on electrical transport data, with assumptions about how that quantity is related to chemical diffusion. For example, it is assumed that electrical transport is controlled only one kind of dominant, majority defect and that this defect is an oxygen vacancy. As discussed below, later work has shown that these assumptions may not be valid for perovskites, and the relationship between oxygen vacancies and diffusion of Ca-Pb is ambiguous.

Reasons for the observed concentration dependent diffusion rates of Pb in $CaTiO_3$

The observation that Pb diffuses at two distinctly different rates above and below a threshold concentration is an intriguing find of this study. We consider several possible scenarios below to arrive at the most likely explanation for this behavior:

Compositional dependence of interdiffusion. Diffusion of Pb^{2+} in Ca-perovskite can be described as a simple interdiffusion process with Ca^{2+}. The corresponding interdiffusion coefficient, D_{Pb-Ca}, is in general a function of the molar fraction of Pb on the Ca site, X_{Pb}, and the respective tracer diffusion coefficients of Pb and Ca, D^*_{Pb} and D^*_{Ca}, respectively. The relationship is given by (e.g. Barrer et al. 1963; Manning 1974; Lasaga 1979):

$$D_{Pb-Ca} = \frac{D^*_{Pb}\, D^*_{Ca}}{X_{Pb}D^*_{Pb}+(1-X_{Pb})D^*_{Ca}}\left(1+\frac{\partial ln\, \gamma^{Prv}_{PbTiO3}}{\partial lnX_{Pb}}\right) \quad , \qquad (2)$$

where γ^{Prv}_{PbTiO3} is the activity coefficient of the $PbTiO_3$ component in perovskite, Prv. The factor within brackets on the right is a thermodynamic factor, which equals unity if the Pb content is in the Henrian domain with a constant activity coefficient. For Pb concentrations reaching minor element level it is potentially possible that this activity coefficient may change considerably and thus be a factor that produces a change in D_{Pb-Ca}. However, the functional form of this relationship is such that it describes a continuous variation of D_{Pb-Ca} with X_{Pb} and it is not possible to obtain a discrete jump in diffusivity at a threshold Pb-concentration, as observed in this study.

Charge neutrality conditions. The increase in diffusivity by two orders of magnitude when the concentration of Pb drops below a threshold value is similar to the behavior recently found for diffusion of Zr, Hf, Nb, and Ta in rutile (Dohmen et al. 2018) and rare earth element (REE) diffusion in olivine (Chakraborty et al. 2018, EMPG abstract, manuscript in preparation). In these studies, the behavior was explained by the *heterovalent* substitution of the diffusing ions into the host lattice, which affects the concentrations of the relevant point defects. However, in the present system Pb^{2+} is presumably incorporated into the perovskite structure by *homovalent* substitution for Ca^{2+}, and hence the charge balance in the crystal is not affected.

Fast diffusion pathways. An alternative explanation for such profile shapes is to attribute the diffusion tail to a diffusion flux along fast diffusion paths such as dislocations by "pipe diffusion" (Le Claire and Rabinovitch 1981). Indeed, we found some areas where the Pb intensity, measured with TOF-SIMS, was higher throughout the whole profile depth (Figure A1). These one dimensional channels, normal to the diffusion interface, are distributed randomly throughout the analyzed area. However, we found no correlation between the density of the domains, visible on the surface, in $CaTiO_3$ (Figure A2), the twin-boundaries, and the lengths of the diffusion profiles. Recalculation of the diffusion profiles without using the signals from the pipes affects only the signal intensity but not the profile shape. Thus, the diffusion coefficients remain unaffected when the effect of the pipes are "filtered out" (Figure 7). Moreover, if the measured concentrations represent an averaged sum of concentrations in the undisturbed bulk and in the pipes, then the threshold concentration at which the diffusion behavior changes would be strongly dependent on the number and size of the pipes, and not be fixed at one specific value C_{crit}, as was found in this study.

Nevertheless, we considered the possibility that the profiles resulted from diffusion in a type A regime (Harrison 1961) where the bulk diffusion coefficient D_{bulk} is the integrated diffusivity in a heterogeneous system with contributions from grain boundaries D_{gb} and the mineral lattice D_l

$$D_{bulk} = f_{gb} D_{gb} + (1 - f_{gb}) D_l \quad . \tag{3}$$

Here f_{gb} is the volume fraction of the grain boundaries. The conditions for the type A regime are satisfied when the diffusion distance L is much larger than $d/2$, where d is the distance between parallel grain boundaries (or other fast diffusion pathways) normal to the diffusion front. Hence, the behavior of such a system is macroscopically similar to diffusion in a homogeneous material. Our microstructural observations show that the distance between the twin-boundaries, $d/2$ (i.e. Figure 6) is larger than L and therefore the requirements for diffusion in a type A regime are not fulfilled.

Diffusion of Pb as multiple species. Another potential explanation for the observed profile shape is the presence of Pb^{4+}, formed by a reaction such as

$$PbO + \frac{1}{2}O_2 = PbO_2 \tag{4a}$$

and incorporated into perovskite

$$PbO_2 + CaO = CaPbO_3\ . \tag{4b}$$

That would require Pb^{4+} to be enriched in the uppermost layers of the $CaTiO_3$-substrate and contribute to the slow diffusion in that layer, while Pb^{2+} would diffuse more efficiently and represent the fast diffusing regime. Pb^{4+} containing oxides (PbO_2 and $Pb_2[PbO_4]$) decompose rapidly at high temperatures and we have no evidence for the presence of Pb^{4+} in any of the samples. Nonetheless, Pb^{4+} could be present as a species in a crystal, but it would require a different diffusion mechanism with a higher activation energy, since Pb^{4+} does not fit well in the perovskite lattice (6-fold Pb^{4+} is 28% larger than 6-fold Ti^{4+}). However, the activation energies we have obtained are very similar and almost identical within error for the slow region (139(32) kJ/mol) and for the fast region (158(24) kJ/mol) (Figure 8). The RBS profile of sample Pv_Pb_31 depicted in Figure 1b shows a rounded Ti-edge. We accounted for this by manually adding a Ti-deficit to match the observed profile. This might imply that Pb diffused into the Ti-lattice site, though, the derived Ds are identical to experiments where we don't see a rounded Ti-edge. The shape of the Ti-edge is probably caused by an analytical artifact. Hence, we have no unequivocal proof for the presence of Pb^{4+}. The possibility of Pb^{4+} in the perovskite structure has to be systematically investigated in a future study.

Lattice strain effects and solute segregation. When Pb^{2+} enters the $CaTiO_3$ lattice there is a large mismatch in size [$\Delta r = (r_{Ca} - r_{Pb}) = 0.15$ Å (Shannon 1976)] and this must cause considerable strain in the lattice. Lattice strain energy resulting from the substitution of a trace element of different ionic size in a crystal lattice has been considered by Nagasawa (1966) and Brice (1975) and adapted for applications to trace element partitioning studies for a wide range of minerals and chemical elements by Blundy and Wood

(1994). For major elements, additional effects come into play because the incorporation of an additional ion with a radius mismatch in a lattice that is already deformed by the incorporation of other such ions is somewhat easier, and these relaxation effects need to be taken into account. Formulations for the calculation of strain energies in such situations have been provided by Christian (1975), Greenwood (1979) and discussed in Ganguly and Saxena (1988). In all of these formulations, the bulk modulus, the shear modulus, and a mismatch parameter squared (either the radius or the volume) play a role. The considerable Young's modulus of 254 GPa (Voigt-Reuss-Hill average calculated with progs.coudert.name/elate/mp?query=mp-4019 (Gaillac et al. 2016)) indicates that even small size mismatches would lead to considerable strain in $CaTiO_3$.

On the other hand, if the strain exceeds a certain value, it is energetically efficient to generate free / disordered surfaces or interfaces to relax the strain. Such relaxation may occur through the formation of features such as dislocations, sub-grain boundaries, or cracks. The strain energy required to generate such discontinuities have been derived subject to many simplifying assumptions (e.g. see Christian, 1975; Carter and Norton 2007), but a general feature of such expressions is that they are of the form $E = \alpha \mu b^2$, where α is a constant that includes the size of the disturbed region, μ is the shear modulus, and b is the Burgers vector in the case of a dislocation, or a suitable length scale in the case of other discontinuities. Once enough strain energy has been accumulated through the incorporation of a misfit ion to equal this energy required to produce a discontinuity, the system relaxes by forming such a discontinuity. This behavior has an important feature that matches with our observed diffusion behavior – discontinuities develop above a critical threshold concentration of the diffusing ion.

As soon as such a discontinuity forms within a crystalline lattice made up of ions, the local electrical neutrality is disturbed at that location, leading to the development of a so-called space charge that then drives a flux of point defects (e.g. vacancies) toward or away from the discontinuity in order to re-establish local charge neutrality (note: vacancies and other defects in an ionic solid are charged entities). A flux of

vacancies, for example, implies a reverse flux of cations. Ultimately, this leads to the discontinuity acting as a sink for such cations, and a high concentration of the relevant cations can develop at these discontinuities. In perovskite structures this effect has been shown to be particularly prominent (e.g. a space charge layer with a potential of 0.1 V across it in $BaTiO_3$, Desu and Payne 1990b, resulting in considerable segregation in grain boundaries, Desu and Payne 1990a). This is consistent with our observation that high concentrations of Pb are observed at the discontinuities (dislocations, defects) in our samples. This aspect explains the high concentration of Pb in the near surface region of our diffusion samples, as well as the slower diffusion rate observed in this region, because many of the Pb ions are "trapped" at the discontinuity.

Thus, based on the observations that (i) the development of discontinuities in $CaTiO_3$ occurs when the concentration of Pb, an ion with a large size mismatch, exceeds a threshold value, (ii) these discontinuities are sites of higher Pb concentration, and (iii) diffusion of Pb in this region is slowed down (a result of "trapping", or binding to the discontinuities to neutralize the space charge associated with them), indicates to us that this provides the most coherent explanation for the observed diffusion behavior. In contrast to the two mechanisms of diffusion of *heterovalent* cations that arise in oxides and silicates due to a concentration dependent change in charge neutrality conditions of point defects (e.g. Zr, Hf, Nb, Ta in Rutile or REE in olivine, see above), the dual mechanism of diffusion arises here even for the diffusion of a *homovalent* cation due to size mismatch and related strain effects.

Note, that the presence of dislocations and lattice strain do not make the diffusion non-Fickian. The observations we made are best described as a macroscopic process that averages over defects and dislocations.

With increasing depth at a given time, the concentration of Pb decreases to drop below the threshold value required for generating the planar discontinuities and faster, "untrapped" lattice diffusion mediated by point defects becomes the sole mechanism. In natural crystals with low concentrations of Pb (several 10s – 100s ppm), this is the mechanism that is likely to operate.

Point Defect chemistry of $CaTiO_3$

The following discussion is only relevant for the fast diffusion regime, where lattice diffusion via point defects is the rate determining mechanism.

Constraints from other physical measurements. Our knowledge of the point defect chemistry of Ca-perovskite is based almost exclusively on measurements of electrical conductivity (e.g. Balachandran and Eror 1982; Balachandran et al. 1982; Zhou et al. 2002; Bak et al. 2004), with some additional information from studies of oxygen diffusion (e.g. Gautasson and Muehlenbachs, 1993) or chemical diffusion rates inferred from electrical conductivity data (e.g. Bak et al. 2004). In general oxygen vacancies, Ca vacancies and Ti interstitials, in addition to electrons in the conductance band and electron holes, are considered to be the major point defects (e.g., Zhou et al. 2002). Electrical conductivity of undoped synthetic $CaTiO_3$ is sensitive to fO_2 where the dependence is negative for reducing conditions and becomes positive for oxidizing conditions (Bak et al. 2004b; Bak et al. 2004). This change in the fO_2 dependence is related to the change from a n-type conductor at reducing conditions to a p-type conductor at oxidizing conditions. Unfortunately, it is not possible to unambiguously distinguish between different types of majority point defect schemes that may dominate the charge balance in $CaTiO_3$. This is because the only available data are based on the change of electrical conductivity with fO_2 (Zhou et al. 2002).

Only for very reducing conditions can it be argued that oxygen vacancies (effectively of doubly positive charge) and electrons are the majority point defects that charge balance each other. For the oxidizing conditions, although it was not possible to unambiguously identify the majority defects, it was shown that ionic conductivity contributes significantly to the total conductivity (Bak et al. 2004) and that oxygen vacancies were likely the major ionic charge carrier. These inferences are in line with the general observation that perovskites are known to have high concentrations of oxygen vacancies, resulting in unusually high diffusion rates for oxygen in this class of material (e.g. Gautasson and Muehlenbachs, 1993

for data on $CaTiO_3$). Note, however, that the activation energy for O-diffusion was found to be around 300 kJ/mol (Gautason and Muehlenbachs 1993; Sakaguchi and Haneda 1996) (Figure 8), which is much higher than the activation energies for electrical conduction in different fO_2 regimes (up to ~ 180 kJ/mol, e.g. Bak et al. 2004b), confirming that ionic conduction is only a part of the total charge transfer mechanism in these perovskites.

Summarizing, although electrical transport may be by a combination of electronic and ionic conduction (Bak et al. 2004b), the nature of fO_2 dependence of conductivity may change at oxidizing vs. reducing conditions (Balachandran et al. 1982; Bak et al. 2004b) and the exact nature of majority defects may remain unclear in many conditions (Zhou et al. 2002), it is apparent that oxygen vacancies play an important role in the defect chemistry at all conditions and that cation vacancies constitute minority defects. The important implication for the diffusion of a cation such Pb^{2+} is that it has to be mediated by minority defects (e.g. cation vacancies) that are coupled to and influenced by changes in concentration of the majority defects (e.g. see discussion in De Souza and Martin 2004; Martin 2007; Xu et al. 2011).

Diffusion mechanism in the lattice based on point defect chemistry. We consider the point defect mechanism of diffusion of Pb based on the defect chemistry inferred from electrical conductivity data. Since Pb^{2+} substitutes for Ca^{2+} on the 12-fold cuboctahedral A-site, vacancies on the A-site are the most likely mediators of diffusion of a large cation such as Pb^{2+} (i.e. we do not consider the unlikely possibility that Pb may occur interstitially). $CaTiO_3$ can incorporate an excess of CaO but in the present work TiO_2 is present in excess in the chemical environment and hence by the coexistence of $CaTiO_3$ and TiO_2 the smallest possible chemical potential for CaO is defined in the system CaO-TiO_2 and no excess of CaO should be expected. Thus, for a vacancy mechanism of diffusion in undoped CaTiO3 in the presence of excess TiO_2, and considering the inferences of Zhou et al., 2012 based on electrical conductivity data, formation of vacancy on the A-site (the Ca-site in $CaTiO_3$) may occur by (Kröger-Vink notation):

$$Ca_{Ca}^{x} + O_{O}^{x} + TiO_2 = V_{Ca}^{''} + V_{O}^{\bullet\bullet} + CaTiO_3 \quad (5)$$

According to the corresponding mass action law the concentration of Ca vacancies, V_{Ca}'', is indirectly proportional to the concentration of oxygen vacancies, $V_O^{\bullet\bullet}$, where the brackets denote the concentration of the respective point defects:

$$K_1 = \frac{\left[V_{Ca}''\right]\cdot\left[V_O^{\bullet\bullet}\right]}{aTiO_2} \tag{6}$$

The concentration of $V_O^{\bullet\bullet}$ is coupled to the concentration of electrons, *n*, according to the reaction:

$$O_O^x = 1/2\,O_2 + V_O^{\bullet\bullet} + 2e', \tag{7}$$

with the mass action law:

$$K_2 = n^2 \cdot \left[V_O^{\bullet\bullet}\right]\cdot\left(fO_2\right)^{1/2}. \tag{8}$$

By combining the two mass action laws we thus obtain an equation that describes the concentration of Ca vacancies as a function of the concentration of electrons, *n*, $aTiO_2$ and fO_2:

$$\left[V_{Ca}''\right] = K_1 / K_2 \cdot n^2 \cdot \left(fO_2\right)^{1/2} \cdot aTiO_2. \tag{9}$$

This relationship leads to several significant inferences about the diffusion of cations mediated by $\left[V_{Ca}''\right]$:

(i) At constant $aTiO_2$, in the very reducing regime (below $\log(fO_2)$ = - 16 bar (~ 1000 °C), *n* is proportional to $(fO_2)^{-1/6}$ and therefore, $\left[V_{Ca}''\right]$ is proportional to $(fO_2)^{1/6}$.

(ii) For any other fO_2-regime *n*, relevant to natural systems, is proportional to $(fO_2)^{-1/4}$ indicating that there is no sensitivity of $\left[V_{Ca}''\right]$ on fO_2.

(iii) If the concentration of $\left[V_O^{\bullet\bullet}\right]$ is large (see above), then the concentration of $\left[V_{Ca}''\right]$ is very low (see Eqn. 6).

The two important implications of these for the diffusion of Pb in natural $CaTiO_3$ are:

(a) at most realistic fO_2 conditions, diffusion rates would not be sensitive to fO_2, and experimental data obtained at relatively oxidizing conditions (e.g. air in this study) may be used to model processes in the mantle and crust. Bak et al. (2004) report electrical conductivity for doped and undoped $CaTiO_3$ for a wide range of oxygen fugacities. The regime relevant to natural samples corresponds to the regime II in the Bak et al. study, where the mobility of electrons is independent of fO_2 as demonstrated above.

and

(b) in view of the fact that cation vacancies are minority defects and their concentrations are likely to be very low (see (iii) above), diffusion of Pb and other cations may occur by a cooperative mechanism, as has been found in other perovskite structures (e.g. see discussions in De Souza and Martin 2004, Martin 2007 and Xu et al. 2011). However, unlike in other perovskites, the activation energies of diffusion of Pb found in this study (~ 130 – 150 kJ/mol) are much lower than the activation energy for O diffusion or diffusion of cations in other perovskite analogs (~ 300 kJ/mol). This points to the fact that transport of Pb in $CaTiO_3$ may be anomalous (it could be related to the strain effects discussed above), and there is a need for further exploration of its diffusion mechanism.

Application to natural systems and closure temperatures

All experiments in this study were carried out at atmospheric oxygen pressures because of the high volatility of Pb under reducing conditions. However, as shown above, this is unlikely to limit the applicability of the dataset to natural samples. For example, the majority of kimberlite magmas formed / crystallized in the range of -4 to +4 relative to the quartz – fayalite – magnetite oxygen buffer (Canil and Bellis 2007), i.e. the range where diffusion rates are expected to be insensitive to fO_2.

Implications for geochronology

The diffusion parameters for the fast diffusion D_{Pb}^{fast} were used to calculate the closure temperature of Pb in $CaTiO_3$ for cooling rates corresponding to processes within a magma chamber and during kimberlite / carbonatite ascent. We applied D_{Pb}^{fast} because natural samples contain only trace levels of Pb in the ppm range. Hence, the concentrations are well within the concentration levels for the fast diffusion regime. Nonetheless, the difference of closure temperatures calculated with D_{Pb}^{slow} is in the order of 40 °C only. The closure temperature is much more sensitive to the change in activation energy of about 10 kJ/mol compared to the change in the pre-exponential factor by 2 log units (as we have obtained for the two diffusion coefficients in the two regimes).

We employed the modified Dodson-model of Ganguly and Tirone (1999) to calculate the closure temperatures. The mean closure temperature is than expressed as:

$$\frac{E_a}{RT_c} = ln\left(\frac{A\prime RT_C^2 D_0}{E_a(dT/dt)_{T_C} a^2}\right) \quad (10)$$

where R is the gas constant, T_C is the closure temperature, E_a the activation energy, dT/dt is the cooling rate in C/Myr, D_0 is the pre-exponential factor and a is the radius of the grain. $A' = e^{G+g}$, with G being the geometric factor (e.g. 4.0066 for sphere). The correction closure function yields g (Fig.2 in Ganguly and Tirone 1999). The typical crystal size of perovskite in groundmass kimberlite and carbonatites is between 20 and 100 µm, therefore, we used an average crystal diameter of 50 µm in our calculations. We selected cooling rates of 0.1 °C/Myr to 1e9 °C/Myr, where the latter corresponds to the rapid cooling of kimberlite magmas during their ascent to the surface (e.g. Peslier et al. 2008). We found that the average closure temperature is ~ 400 °C for slow cooling rates between 0.1 °C/Myr to 100 °C/Myr and ~980 °C for ultra-fast cooling rates of ~1e9 °C/Myr as expected during the ascent of kimberlites (Figure 9).

In addition, we have demonstrated that for a vacancy diffusion mechanism only a small effect is expected at very reducing conditions, below $fO_2 = 10^{-16}$ bar at ~1000 °C. Thus, we do not expect any significant change in the closure temperature at conditions, relevant to the environments of $CaTiO_3$ crystallization in ultrapotassic magmas.

The closure temperatures obtained here at slow cooling rates are significantly lower than the empirical predictions of ~900 °C as reported by Wu et al. (2010). This implies that the model of ionic porosity is not suitable for predicting cationic diffusion parameters for $CaTiO_3$. An indicator that the newly calculated closure temperatures are meaningful is the fact that the ages determined by Rb-Sr in phlogopite are similar to U-Pb perovskite ages (e.g. Smith et al. 1989; Heaman et al. 2003; Batumike et al. 2008; Tappe et al. 2009) from the same samples – this is what would be expected based on the similarity in the diffusion parameters D_0 and E_a (Hammouda and Cherniak 2000). Hammouda and Cherniak (2000) determined the Arrhenius relation of Sr in F-phlogopite parallel to c with $D_{Sr} = 2.7 * 10^{-14} * exp(135.9(3.1)kJ/mol/RT)\ m^2/s$, which is similar to D_{Pb}^{fast} presented above. The corresponding closure temperature for Sr in F-phlogopite is ~ 700 °C along the c-axis. Strong anisotropy of diffusion, however, indicated that for phlogopite the closure temperature calculated for diffusion along the plates is much lower (~ 300 °C, depending on the cooling rate and geometry). In another study, the closure temperature for the Rb-Sr system in phlogopite was calculated to be ~ 435 °C for 1-2 mm large crystals with calcite and plagioclase present as sink for Sr (Willigers et al. 2004). However, in this case the nature of the coexisting minerals plays a role and the numbers cannot be directly compared with the data for $CaTiO_3$. At very fast cooling rates, e.g. during magma ascent in a kimberlite eruption, the closure temperature is similar to the initial magma temperature. As a consequence, the rapid magma ascent does not reset the lead content of the perovskite.

The consequences of the derived closure temperatures can be summarized as follows, (i) the closure temperatures of Sr in phlogopite and Pb in $CaTiO_3$ are nearly identical, therefore, ages obtained from the Rb-Sr and U-Pb geochronometer should yield the same age within the uncertainties in case of slow cooling; (ii) secondary processes, like infiltration of high-temperature metasomatic fluids or late stage metamorphism, will reset the Pb-age, at least partially, (iii) the U-Pb systems remains open until the accent of the kimberlite magma, representing the age of kimberlite eruption and not the age of processes in the deep seated magma reservoir.

Acknowledgements

CB thanks S. Tappe for his valuable input on kimberlite magmatism that improved the manuscript. KM acknowledges the time and help of Dorothea Wiesner and the financial support from DFG MA 6287/3. We thank the editor Julia Hammer and the reviewers Bruce Watson and Michael Jollands for their comments and suggestions that helped to improve the manuscript.

References

Bak, T, Nowotny, J., Sorrell, C., Zhou, M., and Vance, E. (2004) Charge transport in CaTiO 3: I. Electrical conductivity. Journal of Materials Science: Materials in Electronics, 15, 635–644.

Bak, T., Nowotny, J., and Sorrel, C.C. (2004a) Chemical diffusion in calcium titanate. Journal of Physics and Chemistry of Solids, 65, 1229–1241.

Bak, T., Nowotny, J., Sorrell, C.C., and Zhou, M.F. (2004b) Electronic and ionic conductivity in CaTiO 3. Ionics, 10, 334–342.

Balachandran, U., and Eror, N. (1982) Defect struture of lanthanum-doped CatiO3 Vol. 61, pp. 815–815. Presented at the American Ceramic Society Bulletin, American Ceramic Society.

Balachandran, U., Odekirk, B., and Eror, N.G. (1982) Defect structure of acceptor-doped calcium titanate at elevated temperatures. Journal of Materials Science, 17, 1656–1662.

Barrer, R.M., Bartholomew, R.F., and Rees, L.V.C. (1963) Ion exchange in porous crystals: Part II. The relationship between self-and exchange-diffusion coefficients. Journal of Physics and Chemistry of Solids, 24, 309–317.

Batumike, J.M., Griffin, W.L., Belousova, E.A., Pearson, N.J., O'Reilly, S.Y., and Shee, S.R. (2008) LAM-ICPMS U–Pb dating of kimberlitic perovskite: Eocene–Oligocene kimberlites from the Kundelungu Plateau, D.R. Congo. Earth and Planetary Science Letters, 267, 609–619.

Bednorz, J.G., and Müller, K.A. (1986) Possible highT c superconductivity in the Ba− La− Cu− O system. Zeitschrift für Physik B Condensed Matter, 64, 189–193.

Beyer, C., Berndt, J., Tappe, S., and Klemme, S. (2013) Trace element partitioning between perovskite and kimberlite to carbonatite melt: New experimental constraints. Chemical Geology, 353, 132–139.

Blundy, J., and Wood, B. (1994) Prediction of crystal-melt partition coefficients from elastic moduli. Nature, 372, 452–454.

Brady, J.B., and Cherniak, D.J. (2010) Diffusion in minerals: an overview of published experimental diffusion data. Reviews in mineralogy and geochemistry, 72, 899–920.

Brice, J.C. (1975) Some thermodynamic aspects of the growth of strained crystals. Journal of Crystal Growth, 28, 249–253.

Canil, D., and Bellis, A.J. (2007) Ferric iron in CaTiO3 perovskite as an oxygen barometer for kimberlite magmas II: applications. Journal of Petrology, 48, 231–252.

Carter, C.B., and Norton, M.G. (2007) Ceramic materials: science and engineering. Springer Science & Business Media.

Chakhmouradian, A., and Mitchell, R. (2001) Three compositional varieties of perovskite from kimberlites of the Lac de Gras field (Northwest Territories, Canada). Mineralogical Magazine, 65, 133–148.

Chakhmouradian, A.R., Reguir, E.P., Kamenetsky, V.S., Sharygin, V.V., and Golovin, A.V. (2013) Trace-element partitioning in perovskite: implications for the geochemistry of kimberlites and other mantle-derived undersaturated rocks. Chemical Geology, 353, 112–131.

Chandra, A., and Pandey, D. (2011) Evolution of crystallographic phases in the system (Pb1−xCax)TiO3: A Rietveld study. Journal of Materials Research, 18, 407–414.

Cherniak, D. (2000) Pb diffusion in rutile. Contributions to Mineralogy and Petrology, 139, 198–207.

Cherniak, D., and Watson, E. (2001) Pb diffusion in zircon. Chemical Geology, 172, 5–24.

Christian, J.W. (1975) The Theory of Transformations in Metals and Alloys. I. Equilibrium and general kinetic theory, 586.

Corgne, A., and Wood, B.J. (2002) CaSiO3 and CaTiO3 perovskite-melt partitioning of trace elements: Implications for gross mantle differentiation. Geophysical Research Letters, 29.

Costa, F., Dohmen, R., and Chakraborty, S. (2008) Time scales of magmatic processes from modeling the zoning patterns of crystals. Reviews in Mineralogy and Geochemistry, 69, 545–594.

Crank, J. (1979) The mathematics of diffusion. Oxford university press.

De Souza, R.A., and Martin, M. (2004) Secondary ion mass spectrometry: A powerful tool for diffusion studies in solids. Archives of Metallurgy and Materials, 49, 431–446.

Desu, S.B., and Payne, D.A. (1990a) Interfacial Segregation in Perovskites: I, Theory. Journal of the American Ceramic Society, 73, 3391–3397.

——— (1990b) Interfacial Segregation in Perovskites: II, Experimental Evidence. Journal of the American Ceramic Society, 73, 3398–3406.

Dohmen, R., Becker, H.-W., Meißner, E., Etzel, T., and Chakraborty, S. (2002) Production of silicate thin films using pulsed laser deposition (PLD) and applications to studies in mineral kinetics. European journal of mineralogy, 14, 1155–1168.

Dohmen, R., Ter Heege, J.H., Becker, H.-W., and Chakraborty, S. (2016) Fe-Mg interdiffusion in orthopyroxene. American Mineralogist, 101, 2210–2221.

Dohmen, R., Marschall, H.R., Ludwig, T., and Polednia, J. (2018) Diffusion of Zr, Hf, Nb and Ta in rutile: effects of temperature, oxygen fugacity, and doping level, and relation to rutile point defect chemistry. Physics and Chemistry of Minerals.

Edgar, A.D., and Mitchell, R.H. (1997) Ultra high pressure–temperature melting experiments on an SiO2-rich lamproite from Smoky Butte, Montana: derivation of siliceous lamproite magmas from enriched sources deep in the continental mantle. Journal of Petrology, 38, 457–477.

Gaillac, R., Pullumbi, P., and Coudert, F.-X. (2016) ELATE: an open-source online application for analysis and visualization of elastic tensors. Journal of Physics: Condensed Matter, 28, 275201.

Ganguly, J., and Saxena, S.K. (1988) Mixtures and mineral reactions Vol. 19. Springer Science & Business Media.

Ganguly, J., and Tirone, M. (1999) Diffusion closure temperature and age of a mineral with arbitrary extent of diffusion: theoretical formulation and applications. Earth and Planetary Science Letters, 170, 131–140.

Gautason, B., and Muehlenbachs, K. (1993) Oxygen diffusion in perovskite: Implications for electrical conductivity in the lower mantle. Science, 260, 518–521.

George, W.L., and Grace, R.E. (1969) Formation of point defects in calcium titanite. Journal of Physics and Chemistry of Solids, 30, 881–887.

Goodenough, J.B. (2004) Electronic and ionic transport properties and other physical aspects of perovskites. Reports on Progress in Physics, 67, 1915.

Greenwood, H.J. (1979) Some linear and non-linear problems in petrology. Geochimica et Cosmochimica Acta, 43, 1873–1885.

Hammouda, T., and Cherniak, D.J. (2000) Diffusion of Sr in fluorphlogopite determined by Rutherford backscattering spectrometry. Earth and Planetary Science Letters, 178, 339–349.

Harrison, L.G. (1961) Influence of dislocations on diffusion kinetics in solids with particular reference to the alkali halides. Transactions of the Faraday Society, 57, 1191–1199.

Heaman, L., Kjarsgaard, B., and Creaser, R. (2003) The timing of kimberlite magmatism in North America: implications for global kimberlite genesis and diamond exploration. Lithos, 71, 153–184.

Heaman, L.M. (1989) The nature of the subcontinental mantle from SrNdPb isotopic studies on kimberlitic perovskite. Earth and Planetary Science Letters, 92, 323–334.

Heaman, L.M. (2009) The application of U–Pb geochronology to mafic, ultramafic and alkaline rocks: an evaluation of three mineral standards. Chemical Geology, 261, 43–52.

Hodes, G. (2013) Perovskite-based solar cells. Science, 342, 317–318.

Huang, Y.-H., Dass, R.I., Xing, Z.-L., and Goodenough, J.B. (2006) Double perovskites as anode materials for solid-oxide fuel cells. Science, 312, 254–257.

Jaoul, O., Sautter, V., and Abel, F. (1991) Nuclear Microanalysis: A Powerful Tool for Measuring Low Atomic Diffusivity with Mineralogical Applications. In Diffusion, Atomic Ordering, and Mass Transport pp. 198–220. Springer, New York, NY.

Kennedy, B.J., Howard, C.J., and Chakoumakos, B.C. (1999) Phase transitions in perovskite at elevated temperatures-a powder neutron diffraction study. Journal of Physics: Condensed Matter, 11, 1479.

Kótai, E. (1997) RBX, computer methods for analysis and simulation of RBS and ERDA spectra. AIP Conference Proceedings, 392, 631–634.

Kramers, J., and Smith, C. (1983) A feasibility study of U− Pb and Pb− Pb dating of kimberlites using groundmass mineral fractions and whole-rock samples. Chemical Geology, 41, 23–38.

Kühl, S., Düdder, H., Girgsdies, F., Kähler, K., Muhler, M., and Behrens, M. (2017) Perovskites as Precursors for Ni/La2O3 Catalysts in the Dry Reforming of Methane: Synthesis by Constant pH Co-Precipitation, Reduction Mechanism and Effect of Ru-Doping. Zeitschrift für anorganische und allgemeine Chemie, 643, 1088–1095.

Lasaga, A.C. (1979) Multicomponent exchange and diffusion in silicates. Geochimica et Cosmochimica Acta, 43, 455–469.

Le Claire, A., and Rabinovitch, A. (1981) A mathematical analysis of diffusion in dislocations. I. Application to concentration'tails'. Journal of Physics C: Solid State Physics, 14, 3863.

Manning, J.R. (1974) Diffusion kinetics and mechanisms in simple crystals. In Geochemical transport and kinetics Vol. 634, p. 3. Carnegie Inst. Washington 634.

Martin, M. (2007) Oxygen and Cation Diffusion Processes in Oxygen Ion Conductors. Diffusion Fundamentals, 6, 39–1.

Mitchell, R.H., Welch, M.D., and Chakhmouradian, A.R. (2017) Nomenclature of the perovskite supergroup: A hierarchical system of classification based on crystal structure and composition. Mineralogical Magazine, 81, 411–461.

Nagasawa, H. (1966) Trace element partition coefficient in ionic crystals. Science, 152, 767–769.

Peslier, A.H., Woodland, A.B., and Wolff, J.A. (2008) Fast kimberlite ascent rates estimated from hydrogen diffusion profiles in xenolithic mantle olivines from southern Africa. Geochimica et Cosmochimica Acta, 72, 2711–2722.

Reguir, E.P., Camacho, A., Yang, P., Chakhmouradian, A.R., Kamenetsky, V.S., and Halden, N.M. (2010) Trace-element study and uranium-lead dating of perovskite from the Afrikanda plutonic complex, Kola Peninsula (Russia) using LA-ICP-MS. Mineralogy and Petrology, 100, 95–103.

Rothmann, M.U., Li, W., Zhu, Y., Bach, U., Spiccia, L., Etheridge, J., and Cheng, Y.-B. (2017) Direct observation of intrinsic twin domains in tetragonal $CH_3NH_3PbI_3$. Nature Communications, 8, 14547.

Sakaguchi, I., and Haneda, H. (1996) Oxygen Tracer Diffusion in Single-Crystal CaTiO3. Journal of Solid State Chemistry, 124, 195–197.

Schaffer, M., Schaffer, B., and Ramasse, Q. (2012) Sample preparation for atomic-resolution STEM at low voltages by FIB. Ultramicroscopy, 114, 62–71.

Shannon, R.D. (1976) Revised effective ionic-radii and systematic studies of interatomic distances in halides and chalcogenides. Acta Crystallographica Section A, 32, 751–767.

Smith, C., Allsopp, H., Garvie, O., Kramers, J., Jackson, P., and Clement, C. (1989) Note on the U–Pb perovskite method for dating kimberlites: Examples from the Wesselton and De Beers mines, South Africa, and Somerset Island, Canada. Chemical Geology: Isotope Geoscience section, 79, 137–145.

Smith, C.B., Allsopp, H.L., Garvie, O.G., Kramers, J.D., Jackson, P.F.S., and Clement, C.R. (1989) Note on the U–Pb perovskite method for dating kimberlites: Examples from the Wesselton and De Beers mines, South Africa, and Somerset Island, Canada. Chemical Geology: Isotope Geoscience section, 79, 137–145.

Tappe, S., and Simonetti, A. (2012) Combined U–Pb geochronology and Sr–Nd isotope analysis of the Ice River perovskite standard, with implications for kimberlite and alkaline rock petrogenesis. Chemical Geology, 304, 10–17.

Tappe, S., Steenfelt, A., Heaman, L.M., and Simonetti, A. (2009) The newly discovered Jurassic Tikiusaaq carbonatite-aillikite occurrence, West Greenland, and some remarks on carbonatite–kimberlite relationships. Lithos, 112, 385–399.

Veksler, I.V., and Teptelev, M.P. (1990) Conditions for crystallization and concentration of perovskite-type minerals in alkaline magmas. Lithos, 26, 177–189.

Watson, E.B., and Dohmen, R. (2010) Non-traditional and emerging methods for characterizing diffusion in minerals and mineral aggregates. Reviews in Mineralogy and Geochemistry, 72, 61–105.

Willigers, B.J.A., Mezger, K., and Baker, J.A. (2004) Development of high precision Rb–Sr phlogopite and biotite geochronology; an alternative to 40Ar/39Ar tri-octahedral mica dating. Chemical Geology, 213, 339–358.

Wu, F.-Y., Yang, Y.-H., Mitchell, R.H., Li, Q.-L., Yang, J.-H., and Zhang, Y.-B. (2010) In situ U–Pb age determination and Nd isotopic analysis of perovskites from kimberlites in southern Africa and Somerset Island, Canada. Lithos, 115, 205–222.

Xu, J., Yamazaki, D., Katsura, T., Wu, X., Remmert, P., Yurimoto, H., and Chakraborty, S. (2011) Silicon and magnesium diffusion in a single crystal of MgSiO3 perovskite. Journal of Geophysical Research: Solid Earth, 116.

Yabusaki, K., and Sasaki, H. (2002) Specimen Preparation Technique for Microstructure Analysis Using Focused Ion Beam Process. FURUKAWA ELECTRIC REVIEW, 77–82.

Zhao, Z.-F., and Zheng, Y.-F. (2007) Diffusion compensation for argon, hydrogen, lead, and strontium in minerals: Empirical relationships to crystal chemistry. American Mineralogist, 92, 289–308.

Zhou, M., Bak, T., Nowotny, J., Rekas, M., Sorrell, C., and Vance, E. (2002) Defect chemistry and semiconducting properties of calcium titanate. Journal of Materials Science: Materials in Electronics, 13, 697–704.

Figures

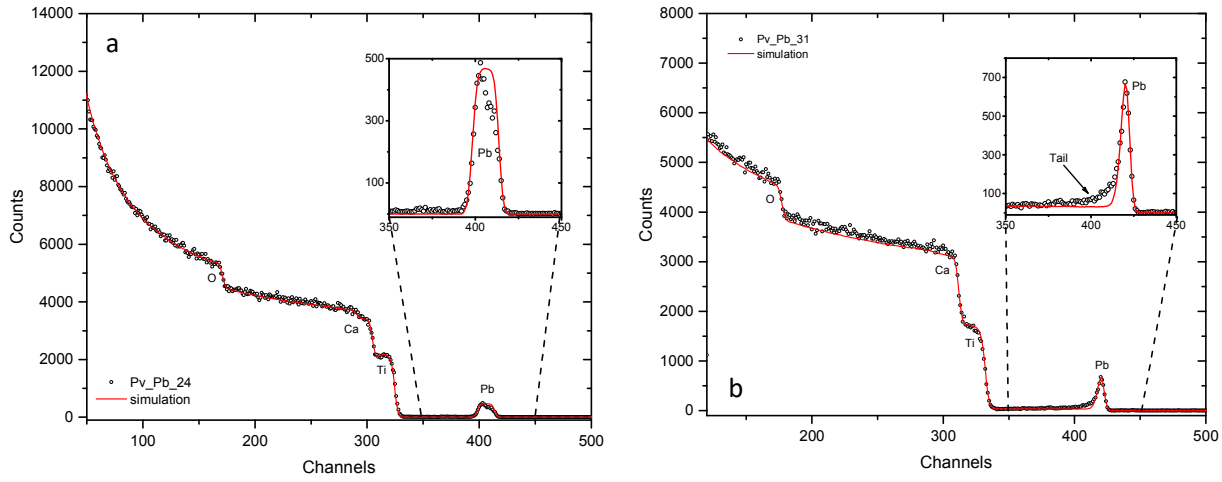

Figure 1 Representative RBS spectra of the thin film experiment Pv_Pb_24 (**a**) and powder source experiment Pv_Pb_31(**b**). Open circles represent the measured α particles and the solid red line represents the simulated profile using a simple error function (see Crank 1979). The magnified profile in the insert of (**a**) shows that some Pb has been lost by evaporation from the surface. The tail was no fitted in the simulation because it involves a concentration dependent diffusion model as discussed below.

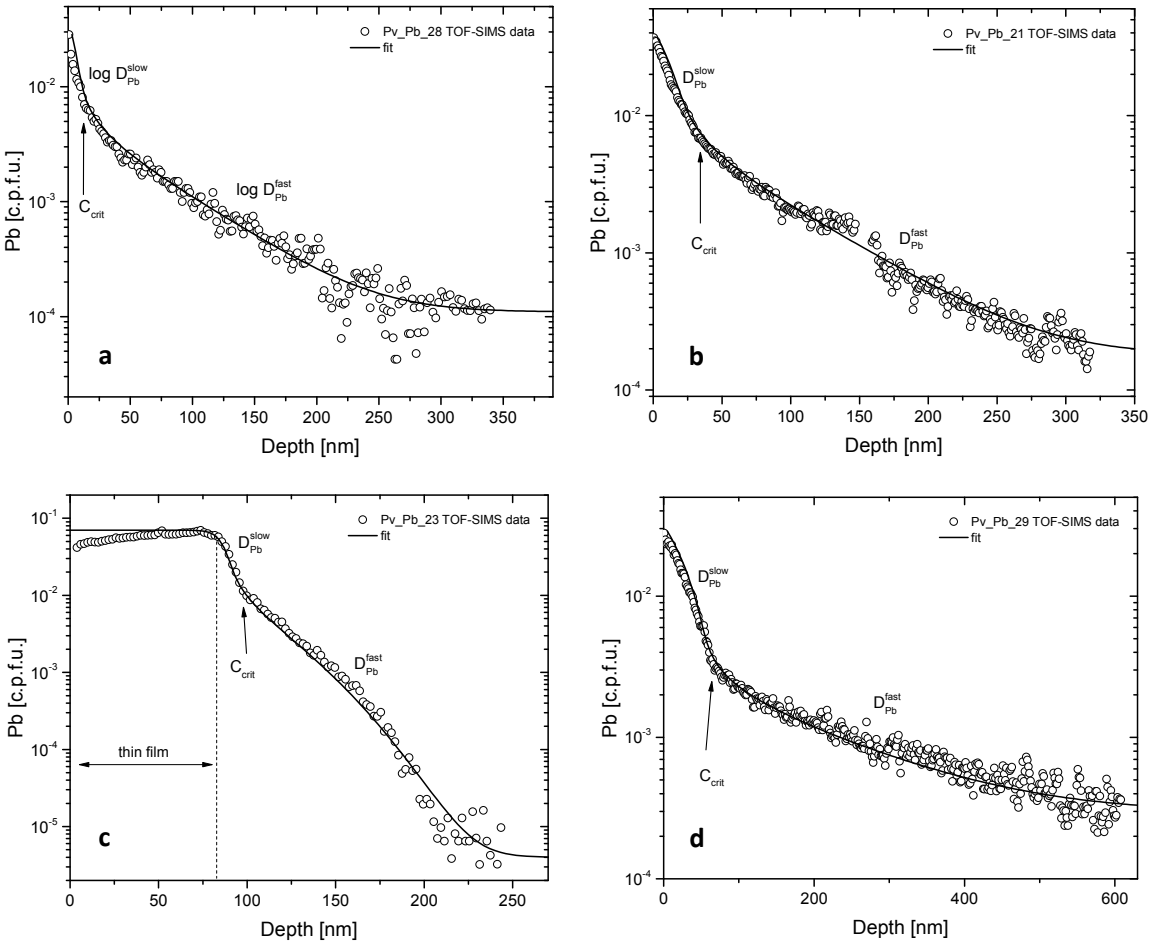

Figure 2 Representative TOF-SIMS Pb-profiles of all experimental setups: (**a**)(**d**) synthetic crystal with powder source, (**b**) natural crystal with powder source and (**c**) thin film on synthetic crystal. Note that the concentrations are plotted on a logarithmic scale here.

605

606

607

608

609

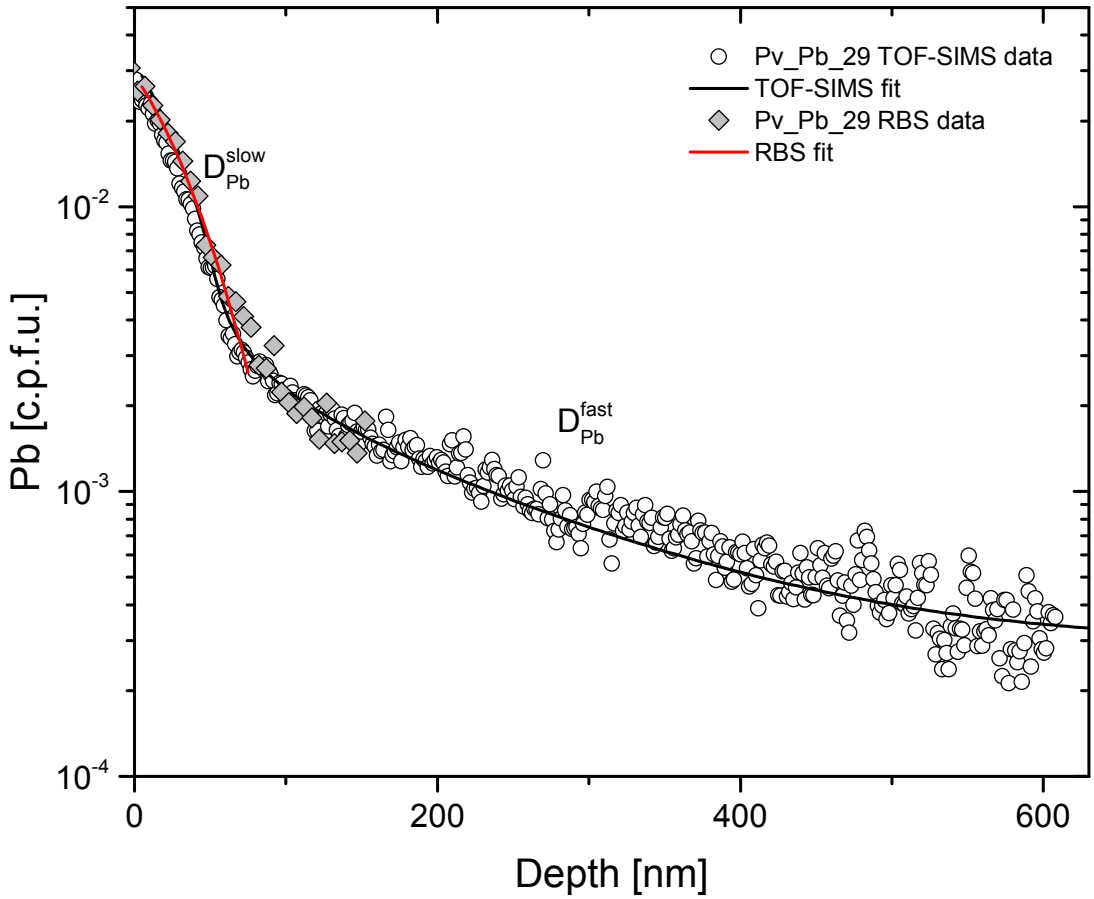

Figure 3 Comparison between RBS (diamonds) and TOF-SIMS (open circles) profiles. The lines represent the fitted diffusion coefficients as reported in Table 2.

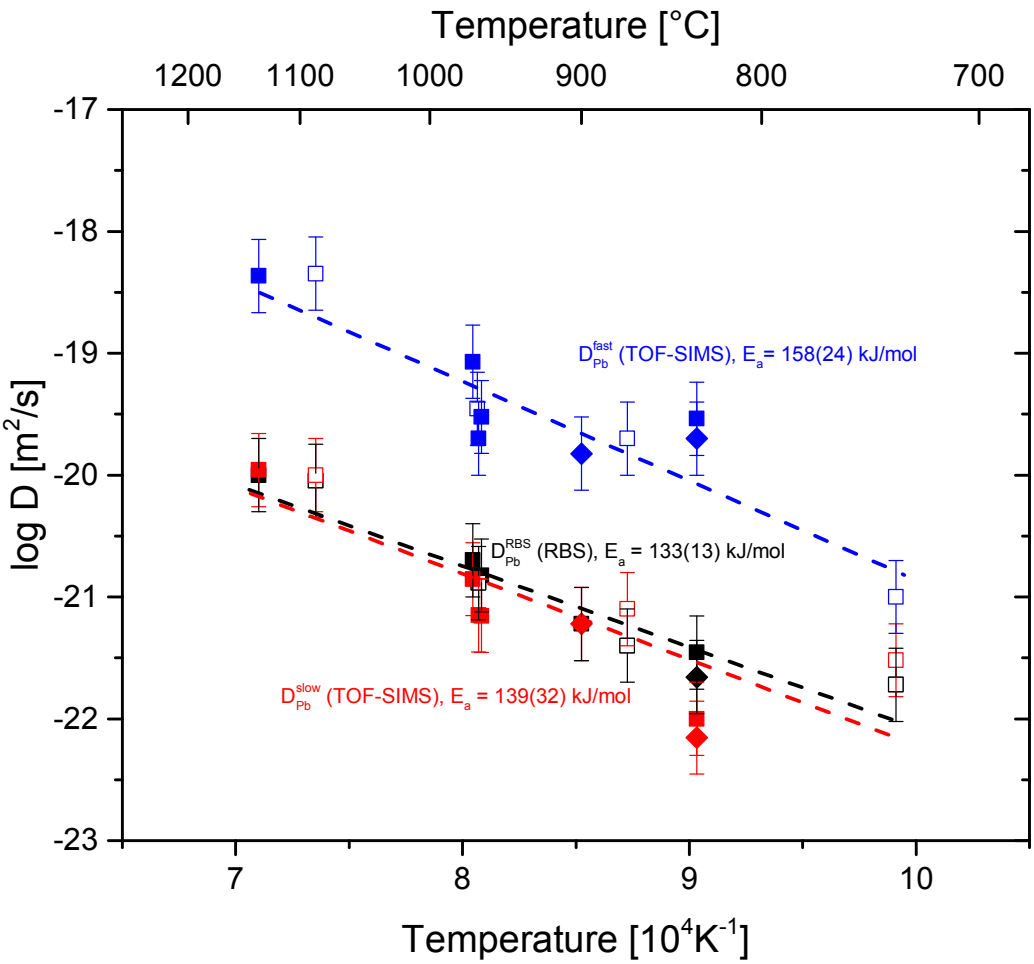

Figure 4 Arrhenius diagram of measured diffusion coefficients. Broken lines represent a weighted linear fit to the diffusion coefficients. Open symbols represent thin film experiments, whereas, solid symbols represent powder source experiments. Diamonds denote diffusion coefficients from natural crystals. The uncertainties are 0.3 log units, as discussed in the text.

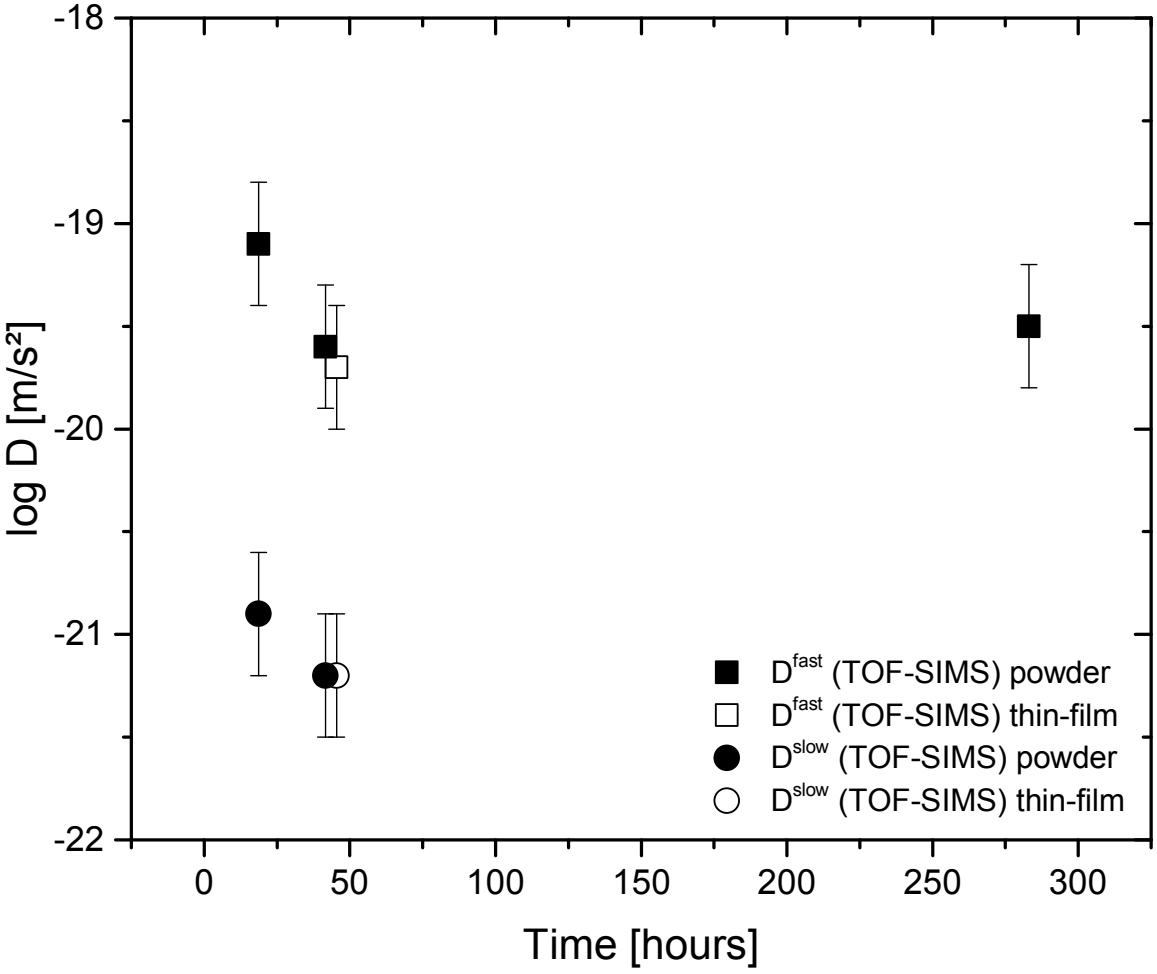

Figure 5 Time series experiments plotted as a function of time in hours. Variations are within the given uncertainties or are attributed to low count rates. The experiments were performed in a temperature range from 964 to 970 °C. The error bars are 0.3 log units as explained in the text.

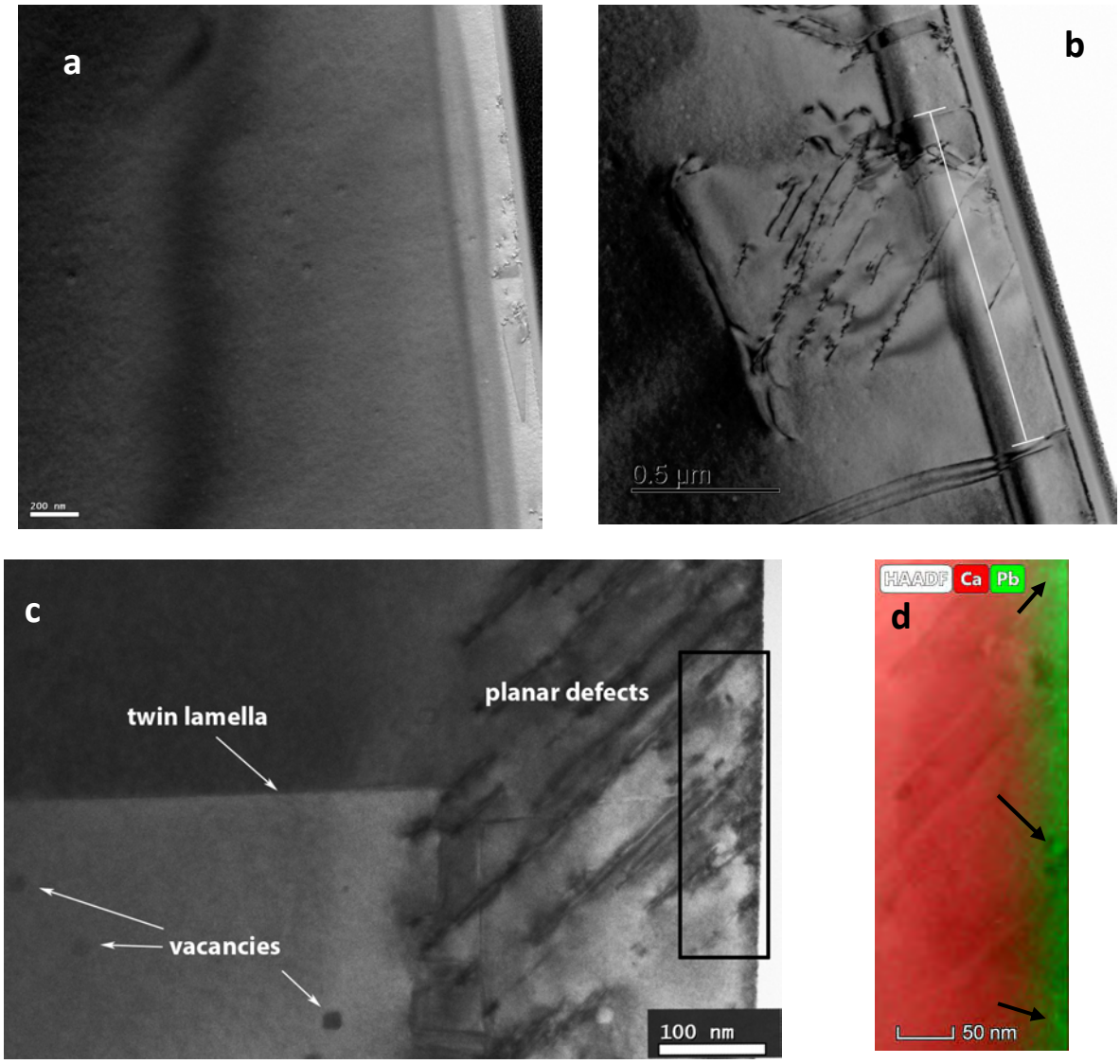

Figure 6 Bright field (BF) image of samples Pv_Pb_29 illustrating the textural features. Surface of the crystal is on the right side on all images. Note, the larger defect concentration is proximity to the surface. (**a**) BF image of a defect-poor area. (**b**) BF image illustrating the distance between the supposed twin lamellae in a defect-rich section. (**c**) Planar defects are only found in proximity to the surface. Large voids of negative crystal shape, supposedly formed by vacancy condensation, are distributed randomly in the bulk of the lamella. Black rectangular represents the area where the EDX map was collected. (**d**) HAADF image with superimposed EDX maps of Ca and Pb. Note, the higher Pb intensity in parts of the surface area. Black arrows highlight areas of higher local Pb-concentrations.

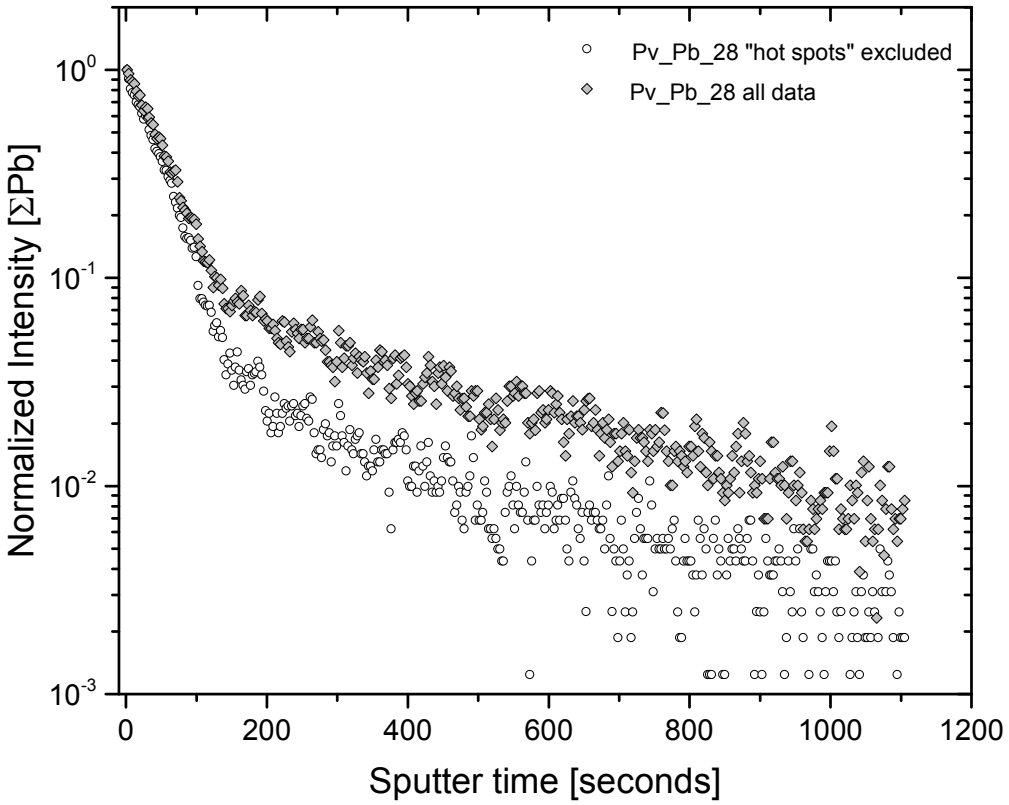

Figure 7 Normalized intensity of the Pb^+-signal shown as a function of sputter time. The diamonds represent the data without exclusion of Pb-rich zones, whereas, the circles represent the same sample with the Pb-enriched areas excluded.

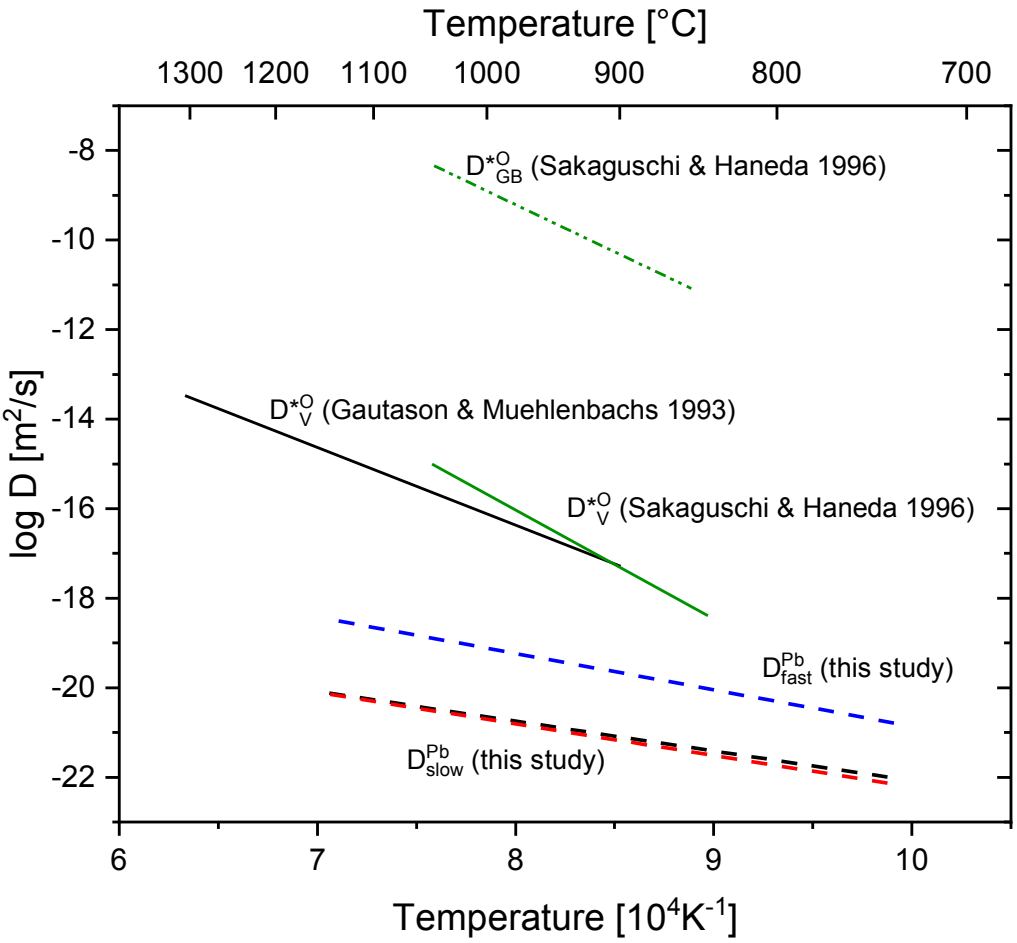

Figure 8 Comparison with other available diffusion data for $CaTiO_3$. Color scheme corresponds to Figure 4.

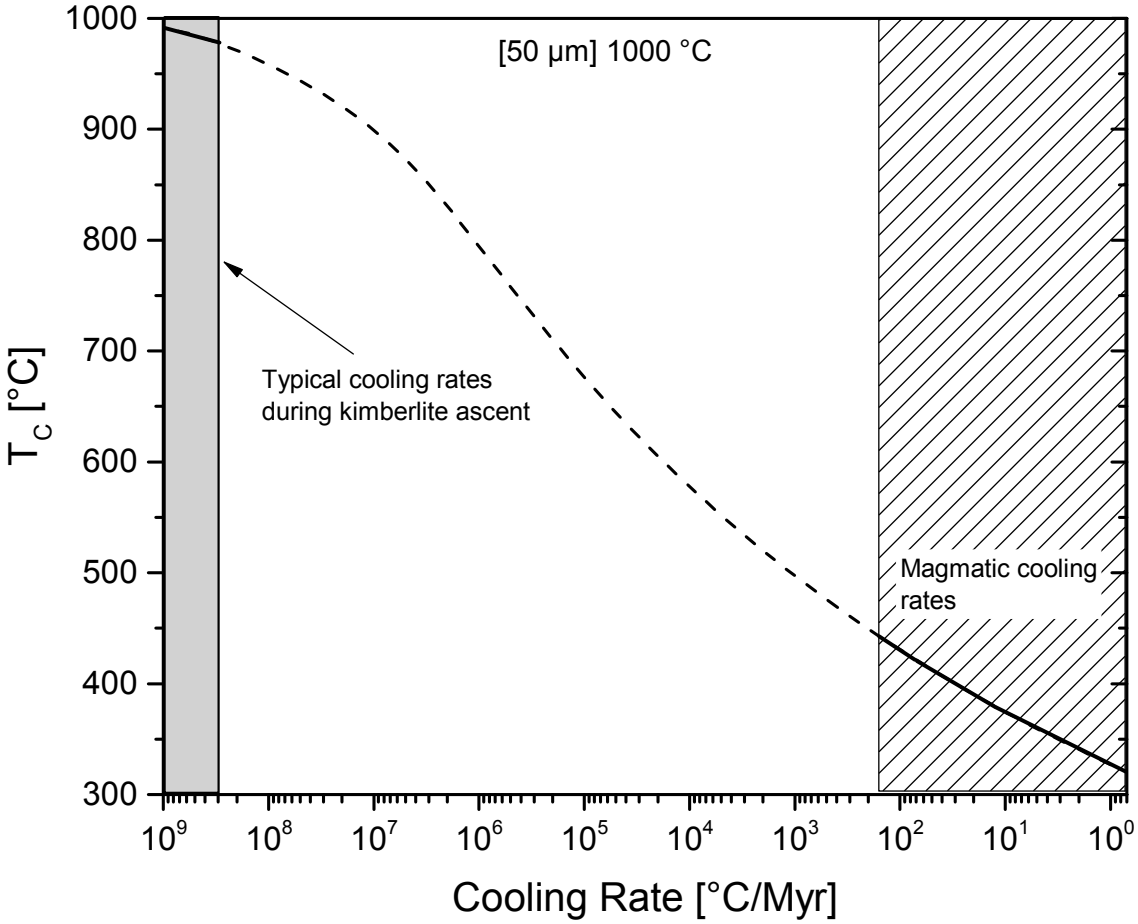

Figure 9 Average closure temperature T_C as a function of cooling rate. The initial magma temperature is 1000 °C and the average grain size is 50 µm. The grey area corresponds to typical cooling rates found in kimberlites, whereas, the banded area represents typical magmatic cooling rates in a deep seated magma reservoir. The striped line represents cooling rates that are not relevant for perovskite parent magmas.

Tables

Table 1 Experimental conditions.

sample	Temp [°C]	Temp [10^4K^{-1}]	Duration [s]	thin film [nm]	dopant	substrate
Thin film						
Pv_Pb_13*				80	$Ca_{0.83}Pb_{0.07}Ti_{1.05}O_3$	(100) synth. $CaTiO_3$
Pv_Pb_22	873	8.73	342000	80	$Ca_{0.83}Pb_{0.07}Ti_{1.05}O_3$	(100) synth. $CaTiO_3$
Pv_Pb_23	736	9.91	928800	80	$Ca_{0.83}Pb_{0.07}Ti_{1.05}O_3$	(100) synth. $CaTiO_3$
Pv_Pb_24	966	8.07	163500	80	$Ca_{0.83}Pb_{0.07}Ti_{1.05}O_3$	(100) synth. $CaTiO_3$
Pv_Pb_25	1087	7.35	7200	80	$Ca_{0.83}Pb_{0.07}Ti_{1.05}O_3$	(100) synth. $CaTiO_3$
Powder source						
Pv_Pb_21	900	8.53	514800	--	$Ca_{0.9}Pb_{0.1}TiO_3$	natural $CaTiO_3$
Pv_Pb_26s	834	9.03	248400	--	$Ca_{0.9}Pb_{0.1}TiO_3$	(100) synth. $CaTiO_3$
Pv_Pb_26n	834	9.03	248400	--	$Ca_{0.9}Pb_{0.1}TiO_3$	natural $CaTiO_3$
Pv_Pb_28	970	8.05	67200	--	$Ca_{0.9}Pb_{0.1}TiO_3$	(100) synth. $CaTiO_3$
Pv_Pb_29	1135	7.10	98100	--	$Ca_{0.9}Pb_{0.1}TiO_3$	(100) synth. $CaTiO_3$
Pv_Pb_30	967	8.06	1018800	--	$Ca_{0.9}Pb_{0.1}TiO_3$	(100) synth. $CaTiO_3$
Pv_Pb_31	964	8.08	150000	--	$Ca_{0.9}Pb_{0.1}TiO_3$	(100) synth. $CaTiO_3$

*Reference sample

Table 2 Calculated diffusion coefficients** obtained from RBS and TOF-SIMS Pb-concentration profiles.

Sample	T[10^4/K]	log[D^{RBS}(m^2/s)] *RBS*	log[D^{slow}(m^2/s)] *TOF-SIMS*	Log[D^{fast}(m^2/s)] *TOF-SIMS*	D^{fast}/D^{slow}
Thin film					
Pv_Pb_22	8.73	-21.3	-21.1	-19.7	1.4
Pv_Pb_23	9.91	-21.7	-21.5	-21.0	0.5
Pv_Pb_24	8.07	-20.9	-21.2	-19.7	1.5
Pv_Pb_25	7.35	-20.0	-20.0	-18.4	1.7
Powder source					
Pv_Pb_21*	8.53	-21.2	-21.2	-19.8	1.4
Pv_Pb_26s	9.03	-21.5	-22.0	-19.7	2.3
Pv_Pb_26n*	9.03	-21.7	-22.2	-19.5	2.6
Pv_Pb_28	8.05	-20.7	-20.9	-19.1	1.8
Pv_Pb_29	7.10	-20.0	-20.0	-18.4	1.6
Pv_Pb_30	8.06		--	-19.5	
Pv_Pb_31	8.08	-20.8	-21.2	-19.6	1.6

Missing data are the consequence of profiles that were too short/noisy to obtain reliable diffusion coefficients. * natural samples. **Uncertainties on diffusion coefficients are ~0.1 log units, based on the reproducibility of the fitting procedure.

Table 3 Pre-exponential factor D_0 and activation energy E_a calculated from the Arrhenius relation.

	log [D_0 (m^2/s)]	**E_a [kJ/mol]**
D_{Pb}^{RBS}	-15.1(6)	133(13)
D_{Pb}^{slow}	-15(1)	139(32)
D_{Pb}^{fast}	-12.4(9)	158(24)